

# Rotor Localization and Phase Mapping of Cardiac Excitation Waves using Deep Neural Networks

Jan Lebert,<sup>1</sup> Namita Ravi,<sup>1,2</sup> Flavio Fenton,<sup>3</sup> and Jan Christoph<sup>1,\*</sup>

<sup>1</sup>*Cardiovascular Research Institute, University of California, San Francisco, USA*

<sup>2</sup>*Yale School of Medicine, Yale University, New Haven, USA*

<sup>3</sup>*School of Physics, Georgia Institute of Technology, USA*

(Dated: September 23, 2021)

The analysis of electrical impulse phenomena in cardiac muscle tissue is important for the diagnosis of heart rhythm disorders and other cardiac pathophysiology. Cardiac mapping techniques acquire numerous local temporal measurements and combine them to visualize the spread of electrophysiological wave phenomena across the heart surface. However, low spatial resolutions, sparse measurement locations, noise and other artifacts make it challenging to accurately visualize spatio-temporal activity. For instance, electro-anatomical catheter mapping is severely limited by the sparsity of the measurements and optical mapping is prone to noise and motion artifacts. In the past, several approaches have been proposed to obtain more reliable maps from noisy or sparse mapping data. Here, we demonstrate that deep learning can be used to compute phase maps and detect phase singularities from both noisy and sparse electrical mapping data with high precision and efficiency. The self-supervised deep learning approach is fundamentally different from classical phase mapping techniques. Rather than encoding a phase signal from time-series data, the network instead learns to directly associate short spatio-temporal sequences of electrical data with phase maps and the positions of phase singularities. Using this method, we were able to accurately compute phase maps and locate rotor cores even from extremely sparse and noisy data, generated from both optical mapping experiments and computer simulations. Neural networks are a promising alternative to conventional phase mapping and rotor core localization methods, that could be used in optical mapping studies in basic cardiovascular research as well as in the clinical setting for the analysis of atrial fibrillation.

**Keywords:** Spiral waves, complex systems, chaos, heart rhythm disorders, phase singularities, rotor mapping

## I. INTRODUCTION

Cardiac muscle cells constantly oscillate between an 'excited' and a 'resting' electrical state, allowing us to assign a phase  $\phi$  to the state of each cell during this cycle. Cardiac mapping and imaging techniques, such as catheter electrode mapping or voltage-sensitive optical mapping, measure the spread of electrical impulses across the heart surface and visualize the spatio-temporal evolution of electrical activity. These visualizations are frequently depicted as phase maps  $\phi(\vec{x}, t)$ , which uniquely represent the time course of the action potential in each location of the tissue and express the synchronicity of the activation in both space and time. Phase maps are particularly suited to characterize the spatio-temporal organization of the electrical wave dynamics underlying cardiac fibrillation [1–6]. During fibrillation, the heart's normal electrophysiology degenerates into a dynamic state driven by chaotic wave phenomena, which propagate rapidly through the heart muscle and cause irregular, asynchronous contractions. These inherently three-dimensional wave phenomena can be observed on the heart's surface using optical mapping, where they often take the shape of rapidly rotating spiral vortex waves or 'rotors'. Phase maps depict these rotors as pinwheel

patterns, with each pinwheel consisting of lines of equal phase that merge at the rotational center of the vortex wave. The topological defect at the vortex's core is referred to as a phase singularity. During ventricular fibrillation, phase singularities move across the heart surface, interact with each other and undergo pairwise creation and annihilation. Phase singularities provide a means to automatically localize and track reentrant vortex waves through the heart muscle. They can be used to track wavebreaks [7, 8], or interactions of vortex cores with the underlying substrate [9], to simplify the visualization of three-dimensional scroll wave dynamics [10, 11], and to measure fluctuations in the complexity of the dynamics [12]. In short, phase singularities are an elegant way to characterize high-frequency arrhythmias that involve reentrant waves, such as ventricular fibrillation (VF) or atrial fibrillation (AF) [13].

Various methods have been proposed to compute phase maps and phase singularities (PS). These methods have been applied to both simulations of VF [10, 11, 14] and AF [15, 16], as well as experimental data, including electrode recordings of VF [4, 5] and AF [17–19] in humans, optical maps of the transmembrane potential during VF [2, 6, 20–22] and AF [23, 24] in isolated hearts, optical maps of action potential spiral waves in cardiac cell cultures [5, 25–27], and time-varying 3D maps of mechanical strain waves measured during VF in isolated hearts using ultrasound [6]. However, phase maps and PS can be prone to measurement artifacts and deficits caused by

---

\* <http://cardiacvision.ucsf.edu/>; [jan.christoph@ucsf.edu](mailto:jan.christoph@ucsf.edu)

inadequate processing of the measurement data, particularly when the data is noisy or sparse [16, 27–31]. Noise and other artifacts, such as motion artifacts, are a frequent issue when analyzing optical mapping recordings [32, 33]. Low spatial resolution or sparsity is associated with multi-electrode arrays in basic research and catheter electrode mapping in the clinical setting, even with multi-electrode catheters, such as 64-lead basket catheters. Mapping fibrillatory wave phenomena at low resolutions can create imaging artifacts and lead to misrepresentations of the underlying dynamics. For instance, classical mapping has been shown to create false positive detections of PS [27–31], contributing to much uncertainty in the imaging-based diagnosis of AF, a field in which rotors remain a highly controversial concept [13, 34]. Mapping of AF would greatly benefit from computational methods, which could account for low spatial resolution and produce reliable visualizations of electrical phenomena from sparse and noisy spatio-temporal electrical signals.

In this study, we demonstrate that deep convolutional neural networks (CNNs) can be used to compute phase maps and phase singularities from short spatio-temporal sequences of electrical excitation wave patterns, even if these patterns are very sparse and very noisy. We use variations of two-stage encoder-decoder CNNs with an encoding stage, a latent space, and a decoding stage, see Fig. 2. The neural network learns to associate electrical excitation wave patterns with phase maps and phase singularity (PS) positions during a training procedure. After training, it is subsequently able to translate electrical excitation wave patterns into phase maps and PS when applied to new, previously unseen data. We tested a modified version of the neural network with an integrated convolutional long short-term memory (LSTM) module in the latent space of the original encoder-decoder architecture. Regardless of the particular architecture, the network was able to predict phase maps and PS in both experimental and synthetic data robustly and with high accuracy. When presented with sparse electrical data from a short temporal sequence of only 1-5 snapshots of electrical activity, the network maintained a robust accuracy level, even in the presence of strong noise. The approach may supersede more classical approaches due to its efficiency, its robustness against noise, and its ability to inter- and extrapolate missing measurement data with only minimal spatial and temporal information.

### A. Phase Mapping and Phase Singularity Detection Techniques

Phase maps and phase singularities (PS) have been used to characterize cardiac fibrillation for over 30 years [1], and various methods were introduced to compute PS either directly or indirectly, see Fig. 1C). In computer simulations, the computation of a phase state or PS is straight-forward as the dynamic variables from the equations describing the local electrical state are read-

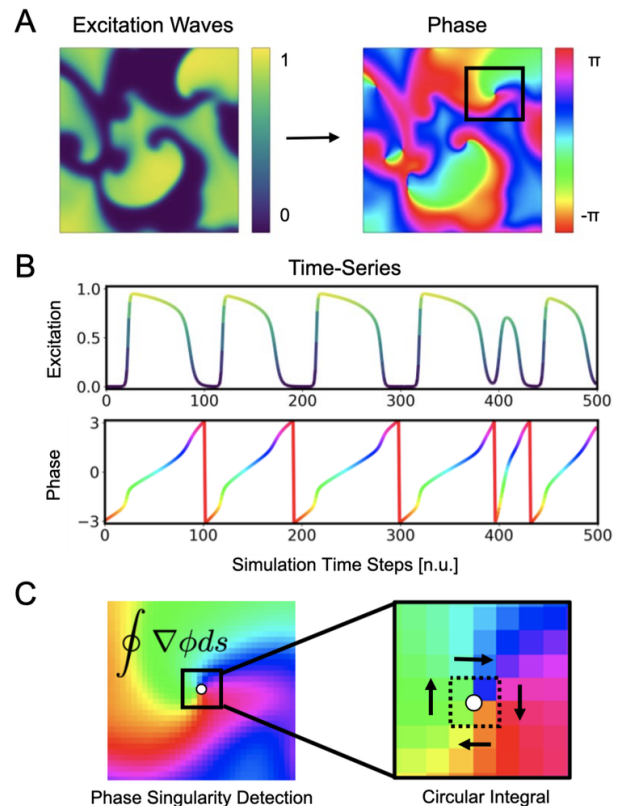


FIG. 1. Cardiac electrical excitation wave pattern and conversion into corresponding phase map for the localization of rotor core positions or phase singularities (PS). A) Simulated electric spiral wave chaos represented by transmembrane potential  $V \in [0, 1]$  (n.u., normalized units) and corresponding phase pattern with phase angle  $\phi \in [-\pi, \pi]$ . B) Time-series data showing a series of action potentials  $V(t)$  and their representation as a phase signal  $\phi(t)$  computed using the Hilbert transform. C) Classical phase singularity (PS) detection [20] using a circular integral ( $2 \times 2$  kernel) for the localization of spiral cores. Here the method is used to generate PS training data for deep learning-based PS detection, see Fig. 2. Detailed field of view of region highlighted by black box in A).

ily available in the simulation and can be used to define a phase angle instantaneously [35]. For instance, with  $V$  and  $r$  for electrical excitation and refraction, respectively, see eqs. (4)-(5), the phase angle can be defined as  $\phi = \arctan2(V, r)$ . Likewise, level-set methods using isocontour lines of two dynamic variables, such as  $V$  and  $r$ , can be used to locate PS directly as the intersection points of these isocontours [36]. However, with experimental data, there is typically only one measured variable, such as the transmembrane voltage or an electrogram, and it is accordingly not possible to define a phase without additional temporal information. With experimental data, it becomes necessary to construct a phase signal  $\phi(t)$  from a single measured time-series  $V(t)$  using techniques such as i) delay embedding [2]:

$$\phi(t) = \arctan2(V(t), V(t + \tau)) \quad (1)$$

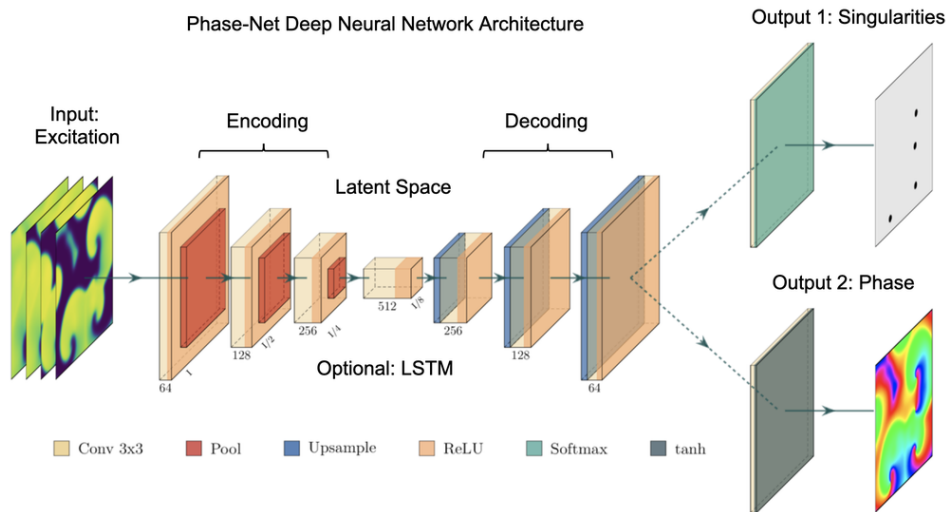


FIG. 2. Deep convolutional neural network (CNN) with encoding stage, latent space and decoding stage for the computation of phase maps and phase singularities (PS) from spatio-temporal maps of electrical excitation. Excitation, phase and PS data is used to train the neural network, which accordingly learns to translate a short sequence of excitation maps into a corresponding phase map or PS coordinates. After training, the network can predict phase maps and PS positions from arbitrary unseen excitation data. We used both a plain convolutional encoder-decoder network architecture and a variant with a long short-term memory (LSTM) neural network module integrated into the latent space. The prediction of phase maps uses a Softmax output activation layer, while the prediction of PS is achieved with a tanh output activation layer. The phase values are trigonometrically encoded as  $x$ - and  $y$ -components, respectively.

with an embedding delay  $\tau$ , which is typically  $\sim 1/4$  of the average cycle length or the first zero-crossing of the auto-correlation function, or ii) the Hilbert transform  $\mathcal{H}(t)$ , which generates the complex analytical signal of a periodic signal from which in turn the phase

$$\phi(t) = \text{Re}(\mathcal{H}(t)) \quad (2)$$

can be derived [21]. The most intuitive approach to compute a time-dependent phase signal  $\phi(t)$  of a sequence of action potentials is to detect the upstrokes of two subsequent action potentials and to define a piecewise linear continuous function  $\phi_L(t)$ , which linearly interpolates the phase angle from  $-\pi$  to  $\pi$  between the two upstrokes. The Hilbert transform generates a phase signal  $\phi_{\mathcal{H}}(t)$  which is very similar to the linearly interpolated phase signal  $\phi_L(t)$ , see Fig. 1B).

Phase singularities can then be calculated, see Fig. 1C), by using the circular line integral method developed by Iyer and Gray [20] summing the gradient of the phase along a closed circular path  $s$  around a point  $\vec{x} = (x, y)$  in the phase plane:

$$\oint \nabla \phi(x, y; t) ds = \pm 2\pi \quad (3)$$

If the circular path is sufficiently small (typically around  $2 \times 2$  pixels), the integral yields  $\pm 2\pi$  when the line integral encloses a phase singularity (the sign indicates chirality), or 0 if it does not enclose a phase singularity. As the line integral method calculates the spatial gradient of the phase, it is very sensitive to noise and requires continuous

and smooth phase maps. Therefore, much work has focused on improving the robustness of phase mapping and PS detection methods under more realistic conditions, e.g with noise or other artifacts that typically occur with, for instance, contact electrode measurements. Zou et al. further refined the line integral method using convolutions and image analysis [32]. Kuklik et al. introduced sinusoidal recomposition to remove undesired high-frequency components during the computation of phase signals using the Hilbert transform [17]. In contrast to the line integration method, Tomii et al. proposed computing the phase variance to locate PS [37]. Similarly, Lee et al. introduced a so-called "location-centric" method to locate PS [38], the method only requiring temporal information about the voltage at the core. Li et al. introduced a Jacobian-determinant method using delay embedding for identifying PS also without explicitly computing a phase [39]. Marcotte et al. [40] and Gurevich et al. [41, 42] introduced level-set methods to compute PS in noisy conditions and demonstrated the robustness of the approach with VF optical mapping data. Vandersickel et al. proposed to use graph theory to detect rotors and focal patterns from arbitrarily positioned measurement sites [43]. Mulimani et al. used CNNs to detect the core regions of simulated spiral waves using a CNN-based classification approach and discriminating sub-regions containing spiral wave tips from areas exhibiting other dynamics, and consequently generated low-resolution heat maps indicating the likely and approximate core regions of spiral waves [44]. Very similarly, Alhusseini et al. used CNNs to classify and discriminate rotational and non-rotational

tiles in maps of AF acquired with basket catheter electrode mapping [45]. Lastly, Li et al. provided a comparison of 4 different PS detection algorithms applied to AF and found that results can vary significantly [46].

## II. METHODS

We developed a two-stage deep convolutional neural network (CNN) with encoder and decoder architecture and trained the network with pairs of two-dimensional maps showing electrical excitation wave patterns and corresponding 'ground truth' phase maps and phase singularity (PS) locations. The training was performed with both simulation data and experimental data, which was obtained in optical mapping experiments during ventricular fibrillation (VF). After training, the network was applied to new data and used to predict phase maps or the positions of PS from unseen excitation wave patterns.

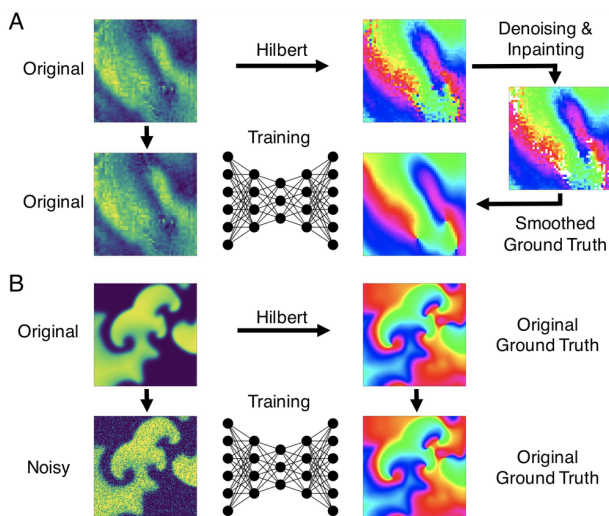


FIG. 3. Preprocessing of data for training of deep learning algorithm for computation of phase maps and phase singularities. A) Preprocessing of noisy optical mapping data: computation of noisy phase maps from raw noisy optical maps using the Hilbert transform. Subsequent denoising using outlier removal, inpainting and smoothing to obtain ground truth phase maps for training. B) Preprocessing of simulation data: computation of ground truth phase maps directly from smooth simulated excitation wave patterns and training with noisy (or sparsified) excitation data.

### A. Neural Network Architecture

The CNN comprises an encoding stage, a latent space, and a decoding stage, see Fig. 2. The neural network is designed to translate an arbitrary two-dimensional electrical excitation wave pattern or a short sequence of two-dimensional excitation wave patterns into a corresponding two-dimensional phase map or predict the positions

of phase singular points in the electrical maps. The prediction of phase maps or PS is performed by two different versions of the neural network, which only differ by training procedure, the activation function in the output layers, and the associated loss function and the training data they are trained on. The phase map prediction neural network is trained with excitation wave patterns as input and a two-dimensional trigonometric encoding of the phase map as target. The trigonometric encoding eliminates the discontinuity present in linear encoding of the cyclic phase  $\phi$  by encoding the value onto a two-dimensional unit circle:  $\phi \rightarrow (\cos(\phi), \sin(\phi)) =: (c, s)$ . The phase map CNN has a two-dimensional layer with two channels as output, which are interpreted as being estimates of the sine  $s_p$  and cosine  $c_p$  of the angle, the predicted phase  $\phi_p$  is decoded as  $\phi_p := \arctan2(s_p, c_p)$ . We use the hyperbolic tangent function as activation function in the phase map neural network for this last step. The PS position estimation neural network is trained with excitation wave patterns as input and a binary class matrix representation of PS positions as target. The target PS are located – by construction – in the center of a  $2 \times 2$  kernel, see Figure 1C). We encode each position by using a binary matrix with the value 1 for all four neighboring pixels and encode the matrix as a class matrix. The PS prediction CNN also has a two-dimensional layer with two channels as output, we use the softmax function as activation function in these layers to convert the two-dimensional values to a probability distribution. We obtain the predicted position of the PS by calculating the center of each connected segment in the dense binary matrix. We implemented and tested two slightly different neural network architectures, both based on a convolutional encoder-decoder architecture. The first network architecture, referred to as model M1, uses a two-dimensional convolutional layer in the latent space, while the second network architecture, model M2, has a two-dimensional convolutional long short-term memory neural layer (LSTM) [47, 48] as the latent space of the CNN. In both models the encoder- and decoder-stage consist of three convolutional two-dimensional convolutional layers, each followed by a batch normalization layer [49], rectified linear unit (ReLU) activation layer [50], and a max-pooling or upsampling layer. The convolutional layers use 64, 128, and 256 kernels in the encoding stage, 512 kernels in the latent space, and 256, 128, and 64 kernels in the decoder stage, see Fig. 2. All network models analyze either a single, static two-dimensional excitation wave pattern or a short sequence of up to 10 excitation wave patterns as input, where the patterns are consecutive snapshots of the activity sampled at equal time intervals in previous time steps, see also section II B. Note that, if we refer to 'video images / frames / excitation patterns' or 'samples', each of these samples may refer to a single or a short series of 2 – 10 two-dimensional excitation patterns. For model M1 the excitation wave patterns are represented as input channels, while for model M2 each excitation wave pattern is processed separately

in the neural network. All neural network models were implemented in Tensorflow [51] version 2.6.0.

## B. Training Data Generation

We generated synthetic training data using a phenomenological computer model of cardiac electrophysiology [52]. In short, nonlinear waves of electrical excitation and refractoriness were modeled using partial differential equations and an Euler finite differences numerical integration scheme:

$$\frac{\partial V}{\partial t} = \nabla^2 V - kV(V - a)(V - 1) - Vr \quad (4)$$

$$\frac{\partial r}{\partial t} = \epsilon(V, r)(kV(a + 1 - V) - r) \quad (5)$$

Here,  $V$  and  $r$  are dimensionless, normalized dynamic variables for electrical excitation (voltage) and refractoriness, respectively. Together with the isotropic diffusive term  $\nabla^2 V = \nabla \cdot (D\nabla V)$  with the diffusion constant  $D = 1.0$  in eq. (4), the model produces nonlinear waves of electrical excitation and the term  $\epsilon(V, r) = \epsilon_0 + \mu_1 r / (V + \mu_2)$  in eq. (5) and electrical parameters  $k$ ,  $a$ ,  $\epsilon_0$ ,  $\mu_1$  and  $\mu_2$  influence properties of the excitation waves. The numerical simulation was implemented in C++ and runs on a CPU and uses multi-threading for parallel computation on multiple cores. The size of the two-dimensional simulation domain was  $200 \times 200$  cells/pixels. The parameters were set to  $a = 0.09$ ,  $k = 8.2$ ,  $\epsilon_0 = 0.01$ ,  $\mu_1 = 0.07$ ,  $\mu_2 = 0.3$  and spiral wave chaos was initiated by applying a series of point stimulations in random locations. With the chosen parameters the dynamics exhibit both chaotic spiral wave and more laminar wave dynamics with strong fluctuations in the complexity of the wave patterns, see Fig. 5F) and Supplementary Movie 1. We generated 20 episodes with a series of 2,500 snapshots of the dynamics in each episode. Fig. 1A) shows an example of such a snapshot. The 2,500 snapshots show about 25 spiral wave rotations. Correspondingly, one spiral rotation is resolved by about 100 snapshots. Note that in the simulation the dynamics are resolved at a  $10 \times$  higher temporal resolution than in the series of snapshots, because we stored a snapshot only in every 10th simulation time step. In total, we obtained 50,000 snapshots, from which we then created 20,000 training samples, where one training sample comprises a short sequence of snapshots with up to 10 images of the excitation. Within the sequence, the first snapshot, denoted with  $t_0$ , corresponds to the snapshot at time  $t$  in the video. The training is performed with the corresponding ground truth phase maps and PS obtained at this time step  $t$  and, correspondingly, the network predicts a phase map or PS for this time step  $t$ . The other snapshots in each sample correspond to snapshots showing the dynamics at previous time steps  $t_{-1}$ ,  $t_{-2}$  etc., where  $t_{-i} = t_0 - i \cdot \tau$  with  $i = 1, \dots, N_t$  and  $N_t$  is the number of snapshots in the sample and  $\tau$  is the temporal sampling distance between the frames over parts of

the previous period. The parameters  $N_t$  and  $\tau$  are discussed in more detail in section III C and in Fig. 10. The training samples were shuffled in time, while the temporal sequence within each sample was kept in its original order. We generated test data which was not used during training by simulating 5,000 snapshots separately using the same electrical parameters and generating samples with the same parameters  $N_t$  and  $\tau$  for testing purposes. We computed ground truth phase maps from the original series of excitation snapshots before shuffling using the Hilbert transform [21] and computed ground truth PS using the Iyer-Gray line integral method [20], as shown in Fig. 1B,C). To simulate noisy excitation wave data, we added noise to the training data, see Fig. 8. The Gaussian noise  $\sigma$ , normally distributed with varying average amplitudes, was added to the individual pixels independently in each frame and independently over time ( $\sigma = 0.1, 0.2, \dots, 0.8$  states the standard deviation of the noise). Each excitation snapshot was optionally further corrupted by deleting excitation values and sparsifying the image for training or testing purposes. All sparsified or deleted values were set to 0.

We generated experimental training data using high-speed video data obtained in optical mapping experiments with voltage-sensitive fluorescent dyes (Di-4-ANEPPS). Imaging was performed during VF in isolated porcine hearts at acquisition speeds of 500fps using a Photometrics Evolve camera ( $128 \times 128$  pixels). The raw optical mapping videos were pixel-wise normalized in time using a sliding-window normalization (window size 120 frames). We used the Hilbert transform to create ground truth phase maps of the pixel-wise normalized optical maps, and the phase maps were subsequently used to compute ground truth phase singularities (PS), see Fig. 3A). Ground truth phase maps and PS and the pixel-wise normalized versions of the voltage-sensitive optical maps containing the original noise (without spatio-temporal smoothing) were used for training. The training data included 25,000 samples, each sample including a short series of voltage-sensitive maps of action potential wave dynamics in analogy to the simulation data. Because the resulting experimental phase maps contain noise, we created smoothed ground truth phase maps by removing outliers using a phase coherence filter, see Fig. 3A). The phase coherence filter involves converting every real-valued phase value into its complex decomposition:

$$\phi(x, y; t) \rightarrow \cos \phi(x, y; t) + i \cdot \sin \phi(x, y; t) \quad (6)$$

and computing the Kuramoto order parameter  $r(x, y; t)$  in every pixel at every time step:

$$r \cdot e^{i\phi} = \frac{1}{N} \sum_i^N e^{i\phi_j} \quad (7)$$

over the complex-valued phase values within a small disk-shaped region including  $j = 1, \dots, N$  complex phase values around each pixel of the noisy complex phase map.

Phase values with  $r < 0.9$  were deleted and interpolated from the remaining surrounding complex phase values. PS were then computed from the smoothed ground truth phase maps in the same way as with the simulation data.

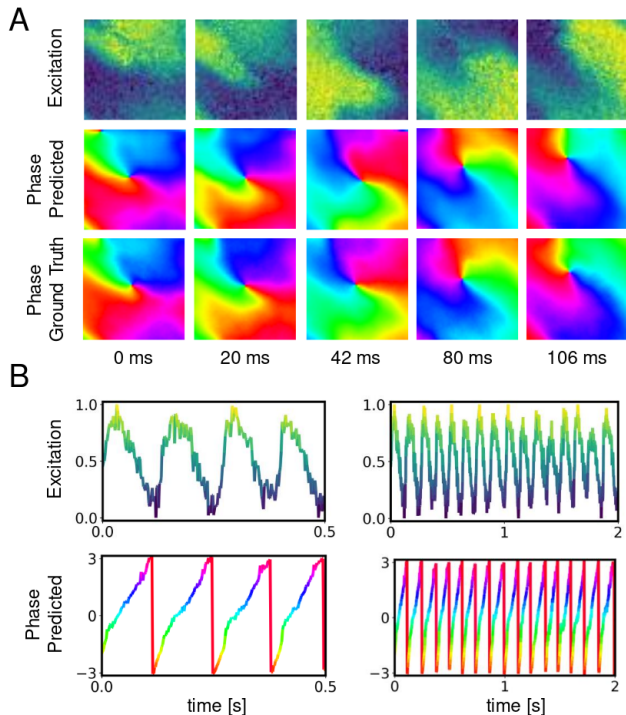


FIG. 4. Deep neural network-based prediction of phase maps from optical maps measured using voltage-sensitive fluorescent dye Di-4-ANEPPS during ventricular fibrillation on surface of isolated heart. A) Optical maps of transmembrane voltage showing counter-clock-wise rotating action potential spiral vortex wave (normalized units  $[0,1]$ , pixel-wise normalization, yellow: depolarized tissue, blue: refractory tissue). Comparison of predicted (top) and ground truth (bottom) phase maps with high qualitative and quantitative agreement. The phase prediction accuracy is  $97\% \pm 6\%$  and the predicted and ground truth phase maps are hard to distinguish. The data was not seen by the network during training. B) Exemplary time-series from a single pixel showing transmembrane voltage  $V(t)$  and predicted phase  $\phi_p(t)$ , respectively.

### C. Training Procedure

Using the simulated data and the experimental data described in section II B, we generated training datasets consisting of corresponding two-dimensional electrical excitation wave data and phase maps as well as  $(x, y)$  positions of PS in these maps. Data-augmentation was not performed and not necessary due to the availability of sufficiently large training datasets. The simulated data was resized from  $200 \times 200$  pixels to  $128 \times 128$  pixels to match the size of the experimental data. The training data was specifically not used during the final prediction, which were performed on a separate dataset, which

was not part of the training. All datasets used for the evaluation (e.g. determining the predictions' accuracy) were separate datasets in order for the network to always exclusively estimate phase maps and PS from data that it had not already seen during training. A fraction of 5% of the frames of the training datasets were used for testing during training. The networks were trained with a batch size of 32 using the Adam[53] optimizer with a learning rate of 0.001 and mean squared error as loss function for the phase map prediction CNN, and categorical crossentropy as loss function for the PS position CNN. All models were typically trained for 10 epochs, if not stated otherwise. With model M1, the training procedure takes roughly 20 seconds per epoch or 3–5 minutes in total with  $\sim 20,000 - 25,000$  frames or samples, respectively. With model M2, the training procedure takes roughly 120 seconds per epoch or 15–20 minutes in total with the same number of frames or samples, respectively. Training and predictions were performed on a NVIDIA GeForce RTX 3090 graphics processing unit (GPU).

### D. Phase Mapping and Rotor Localization Accuracy

The phase prediction accuracy was determined by calculating the angular accuracy,  $1 - \langle \Delta \phi \rangle / \pi$ , where  $\langle \Delta \phi \rangle$  is the average absolute angular difference:

$$\langle \Delta \phi \rangle = \frac{1}{N} \sum |(\phi_p(x, y, t) - \phi_g(x, y, t)) \bmod 2\pi| \quad (8)$$

and  $\phi_p$  is the predicted phase map,  $\phi_g$  is the ground truth phase map computed using the Hilbert transform, and  $N$  is the total number of pixels or phase values over all time steps. With simulation data, the ground truth phase maps and PS were computed from the original simulation data without noise and sparsification using the Hilbert transform. With experimental data, the ground truth phase maps and PS were computed from the original noisy optical maps with subsequent spatial smoothing comprising outlier detection and interpolation, see section II B. The PS prediction accuracy was evaluated by calculating the precision, recall, and F-score from the number of true positive  $tp$ , false positive  $fp$  and false negative  $fn$  predictions. A true positive estimated PS position is counted if any estimated PS location is within at most  $r$  pixels from the ground truth PS. A false positive is counted if no ground truth PS is located within a distance of  $r$  from the estimated PS position. A false negative is counted if a ground truth PS does not have any estimated PS within a distance of at most  $r$ . We chose  $r = 3$  pixels, see also Fig. 5E). Precision is  $tp/(tp + fp)$ , the proportion of estimated PS locations that are close enough to a ground truth PS location. Recall is  $tp/(tp + fn)$ , the proportion of the true phase singularities the neural network is able to detect. The F-score is the harmonic mean

of precision and recall:

$$F\text{-score} = 2 \cdot \frac{\text{precision} \cdot \text{recall}}{\text{precision} + \text{recall}} \quad (9)$$

### III. RESULTS

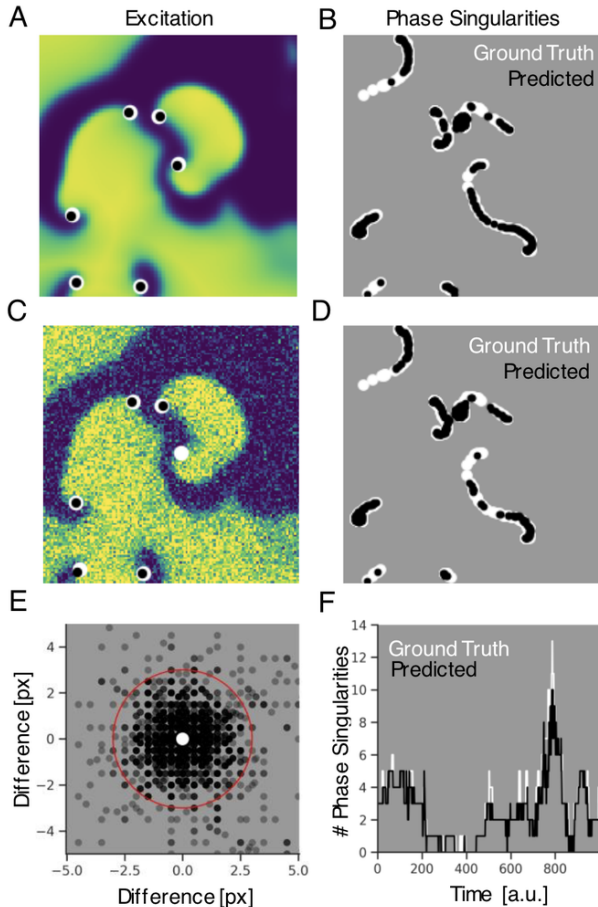


FIG. 5. Phase singularities (PS) predicted by neural network from noisy maps of electrical excitation. White: ground-truth or true PS. Black: predicted PS. A) Electrical spiral wave chaos ( $128 \times 128$  pixels) without noise with PS superimposed indicating positions of spiral wave tips. B) Trajectories of ground truth (white) and predicted (black) PS without noise. C) Electrical spiral wave chaos with noise ( $\sigma = 0.2$ ) with PS superimposed indicating positions of spiral wave tips. D) Trajectories of ground truth (white) and predicted (black) PS with noise. Increase in false negative predictions with noise. E) Spatial mismatch of predicted PS (black) and ground truth PS (white, center). All predicted PS not within 3 pixels (red circle) from true PS are false positives. F) Number of PS over time.

We found that deep encoding-decoding convolutional neural networks (CNNs) can be used to compute phase maps and phase singularities (PS) directly from excitation wave patterns almost instantaneously. The prediction of phase maps can be performed very robustly and

accurately ( $\sim 90-98\%$ ) with both experimental and simulated data, even when the electrical excitation patterns are extremely noisy or sparse, see Figs. 4-10. The direct prediction of PS is sensitive to and adversely affected by noise and sparsity, but performs well with mild noise and non-sparse data.

Fig. 4 and Supplementary Video 1 show predictions of phase maps with voltage-sensitive optical mapping video data, the videos showing action potential spiral vortex waves during ventricular fibrillation (VF) on the left ventricular surface of a porcine heart. Panel A) shows raw pixel-wise normalized optical maps with a counter-clockwise rotating action potential spiral vortex wave (close-up,  $48 \times 48$  pixels cutout from original video image, normalized units  $[0,1]$ , yellow: depolarized tissue, blue: refractory tissue). The action potential rotor performs one rotation in about 110ms. The phase maps in the second and third row show the predicted phase maps  $\phi_p$  obtained with model M1 and ground truth phase maps  $\phi_g$ , respectively. The action potential rotor is characterized by a pinwheel pattern in the phase maps and lines of equal phase merge at the center indicating the spiral wave's core. Predicted and ground truth phase maps are visually almost indistinguishable and exhibit only minor discrepancies. The data was not seen by the neural network previously during training. The predicted phase maps are smooth even though the optical maps displaying the action potential wave patterns are noisy. The neural network predicts also more complicated wave patterns including multiple rotors or phase singularities accurately. On average, the accuracy of the phase prediction with model M1 is  $97\% \pm 6\%$  in terms of angular accuracy evaluated over 3,900 frames. With the LSTM-model M2 the angular accuracy is only  $90\% \pm 16\%$  evaluated over the same data. Fig. 4B) shows an optical trace of a series of action potentials and the corresponding predicted time-series of the phase, which was obtained from the sequence of predicted phase maps in A) using model M1. Even though the predictions were made independently at each time step, the time-course of the predicted phase signal  $\phi_p(t)$  is smooth. Analyzing a short sequence of  $N_t = 5$  optical maps, the neural network provides phase map predictions, which are sufficiently smooth in both space and over time, and the predictions can be retrieved in real-time at an acquisition speed of 500fps. While it would be possible to determine PS locations from the predicted phase maps using classical techniques [20], we did not succeed to predict PS positions reliably in the experimental data directly.

To better understand the behavior of the neural network and evaluate the performance of the phase and PS prediction more systematically, we applied the neural network model M1 to different simulated data and varied input parameters, such as the noise level or the degree of missing data, which we refer to as sparsity. Fig. 5 and Supplementary Video 2 show PS predicted by the neural network analyzing simulated electrical excitation wave patterns without and with noise ( $\sigma = 0.3$ ), respec-

tively. Panels A) and C) show predicted PS (black) and ground truth or true PS (white) superimposed onto the corresponding electrical excitation wave maps. The predictions were obtained with the basic network model M1 with tanh output layer, see section II A. Both predicted and ground truth PS equally indicate the tips or core regions of spiral waves. However, with noise one of the PS was not detected by the network (false negative). Panels B) and D) show the trajectories of the predicted and true PS over a short time frame, without and with noise ( $\sigma = 0.3$ ), respectively. The positions and trajectories of the PS predicted by the neural network co-localize and co-align with the true PS's positions and trajectories, accurately describing the motion of the cores or tips of the spiral waves. The predictions were obtained from a short sequence of 5 excitation frames, c.f. Fig. 10A). The trajectories demonstrate that PS are only predicted in locations where true PS are located. However, some ground truth PS are not predicted by the network and we counted these mispredictions as false negatives. Note that with noise, the number of predicted PS appears to decrease and false negative predictions appear to become more likely. Panel E) shows the spatial distribution of mismatches between true and predicted PS, where the positions of the predicted PS are plotted relative to the position of the true PS at the center. Most predicted PS lie within a radius of 2.5 pixels (red circle) from the true PS and approximate their positions with sub-pixel resolution accuracy. Phase singularities outside this radius were counted as false positives. Note that PS positions are stated with sub-pixel resolution as they were calculated by weighing multiple pixel positions predicted by the network for each PS, see methods. In many cases the prediction matches exactly the position of the true PS, which is originally given at a full pixel resolution. The episode shown in Fig. 5 consists of 5,000 frames with 17,360 true PS in total. Without noise, 16,138 true positive PS are estimated, 251 false positives and 1,205 false negatives, yielding a precision of 98% and recall of 93%, respectively. With noise  $\sigma = 0.2$ , the number of true positives is 14,876, with 198 false positives and 2,538 false negatives, yielding a precision of 99% and recall of 85%, respectively. This corresponds to a F-score of 96 without noise and 92 with noise. With increasing noise, the false positive rate increases and the neural network misses many PS, which might be the reason why the network detects only very few PS with the experimental data. The number of PS over time shown in panel F) also reflects the rather conservative predictions of the network. While the predicted number of PS (black) follows the number and fluctuations of true PS (white), it is occasionally slightly off by about  $\pm 1$  PS and consistently slightly underestimates the number of true PS (here shown for noise  $\sigma = 0.2$ ).

The prediction of phase maps from electrical excitation wave maps is shown in Figs. 6-7 and Supplementary Videos 3-4. Fig. 6A) shows the prediction of a phase map given noisy ( $\sigma = 0.3$ ) electrical excitation wave pat-

terns as input. The predicted phase map  $\phi_p(x, y, t_p)$  is visually almost indistinguishable from the true ground truth phase map  $\phi_g(x, y, t_p)$  shown as a reference on the left and was predicted with an angular accuracy of  $\Delta\phi = 97\%$ . The ground truth phase map  $\phi_g$  was computed from the original electrical excitation wave pattern without noise ( $\sigma = 0.0$ ) using the Hilbert transform and computing in each pixel individually a phase signal from time-series data  $V(t)_{x,y} \rightarrow \phi(t)_{x,y}$  as shown in Fig. 1. By comparison, if the phase map is computed from the noisy electrical excitation data using the Hilbert transform, then the phase map also contains a considerable amount of noise, see lower row in panel A) in Fig. 6. The predictions by the neural network are smooth even though it receives noisy input, and they remain smooth with higher input noise, see also section III A and Fig. 8. All phase predictions  $\phi_p(x, y, t_p)$  shown in Figs. 6 and 7 were obtained with a short spatio-temporal sequence of  $N_t = 5$  electrical excitation wave maps  $V(x, y, t = t_0, t_{-1}, t_{-2}, t_{-3}, t_{-4})$ , where  $t_0 = t_p$  is the prediction time (here shown for  $t_p = 415$  in simulation time steps) and  $t_{-i} = t_p - \tau \cdot i$  are the sampling times (here shown for  $t = 395, 400, 405, 410, 415$  in simulation time steps) with  $\tau = 5$  and  $i = 1, 2, \dots, N_t$  and  $N_t = 4$ . The parameters  $N_t$  and  $\tau$  correspond to the number of sampled electrical excitation maps used for the prediction and the sampling delay, the time between the frames that were sampled, respectively. Their influence on the prediction accuracy is discussed in more detail in section III C and in Figs. 9 and 10. Fig. 6B) shows the prediction of a phase map  $\phi_p(x, y, t_p)$  given the same noisy, but now also in addition sparsified, electrical excitation wave pattern as in A). The sparsification consists of omitting data outside of disk-shaped regions aligned on a grid (values were set to 0), mimicking recordings from a multi-electrode array or an array of fiber optics. The  $7 \times 7$  disks are each 15 pixels in diameter and their center points are 16 pixels apart. As a result of the sparsification, only 43% of the data can be analyzed by the neural network. Despite the sparsification, the network is able to predict the corresponding phase map smoothly and it interpolates the missing data highly accurately. The angular accuracy remains very high at 95% and it is hard to identify differences between the true and predicted phase maps by visual inspection. Figs. 6C) and 7 show predictions of phase maps  $\phi(x, y, t_p)$  obtained with the same underlying excitation wave pattern, but given an even higher degree of sparsification. The disk-shaped measurement regions are aligned in a star-shaped or circular configuration instead of on a grid, covering only 13% and 17% of the area, respectively. With the sparsification pattern in Fig. 6C), the prediction accuracy drops to 88%, but, overall, the predicted phase map still resembles the true phase map and its topology relatively well. The resulting phase map recapitulates the PS at the center but lacks the other and falsely introduces new PS towards the tissue boundary. Nevertheless, the data is also more sparse in these regions. Fig. 7 shows the temporal evolution of

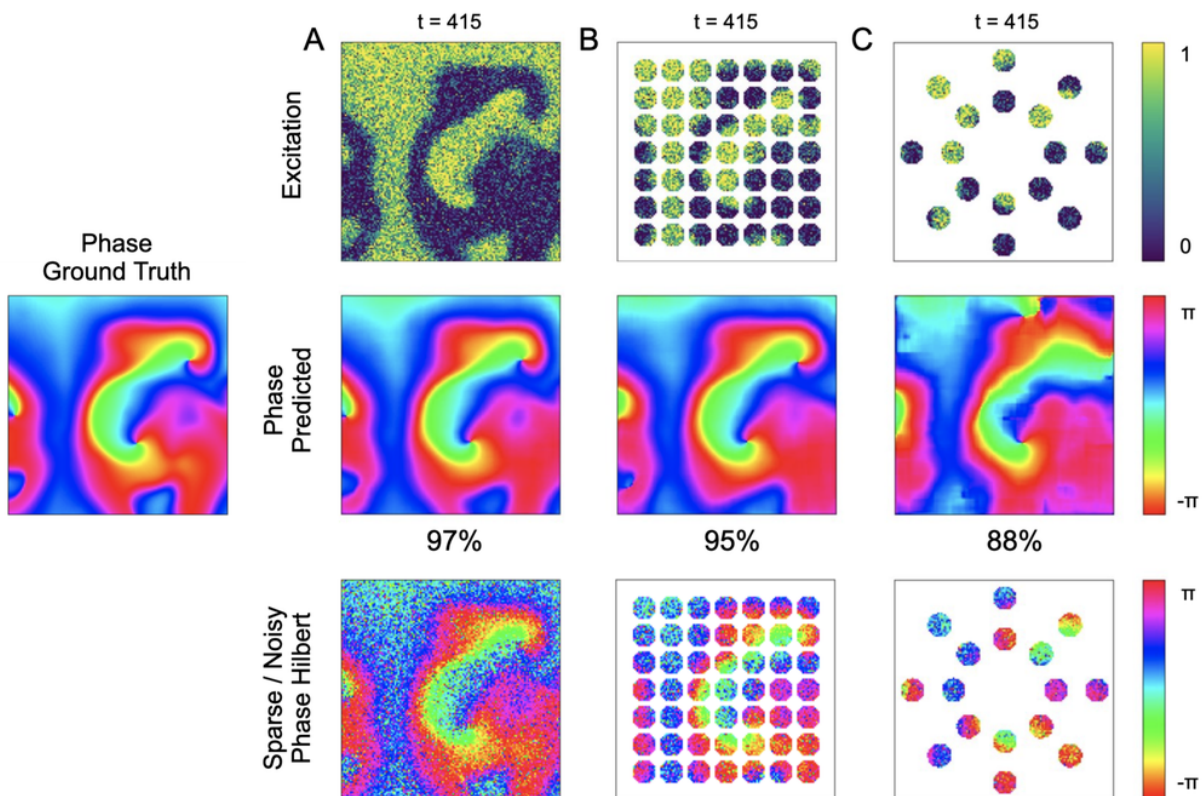


FIG. 6. Deep learning-based prediction of phase maps from noisy and/or sparse electrical excitation wave patterns. Phase maps  $\phi_p(x, y, t_p)$  were predicted from a short spatio-temporal sequence of 5 electrical excitation wave maps  $V(x, y, t = t_1, t_2, t_3, t_4, t_5)$ , A-C). Left: Ground-truth phase map  $\phi_g(x, y)$  calculated from original electrical excitation wave pattern without noise via the Hilbert transform, as shown in Fig. 1A,B). A) Prediction of phase map  $\phi_p(x, y)$  with 97% angular accuracy from noisy electrical excitation wave pattern with noise level of  $\sigma = 0.3$ . The predicted phase map  $\phi_p$  is visually indistinguishable from the true phase map  $\phi_g$ . The data was not seen before by the network during training. B) Prediction with 95% angular accuracy with sparsified electrical excitation wave pattern using a grid electrode pattern (43% coverage). C) Prediction with 88% angular accuracy with sparsified electrical excitation wave pattern using a circular electrode or fiber optic pattern (16% coverage).

phase predictions with a slightly denser multi-electrode catheter-like pattern. The angular accuracy is with 91% a bit higher than with the previous sparsification pattern in Fig. 6C) and both PS at  $t = 415$  and all three central PS at  $t = 430$  are correctly recapitulated by the network. The quality of the phase map predictions allows the computation of the positions of PS just as well as through the direct predictions of PS shown in Fig. 5. As expected, prediction accuracies are lower when the network analyzes sparse patterns than non-sparse patterns. The predictions were obtained with the basic network model M1 with Softmax output layer, see section II A.

Taken together, these results demonstrate that phase singularities and phase maps can be predicted with high accuracies directly from noisy and sparsified maps of electrical excitation. Even if the direct prediction of PS underestimates the number of PS and is less robust than the phase prediction, the predicted phase maps can be used as a back-up to calculate the positions of PS using, for instance, the classical approach by [20] shown in Fig. 1C).

### A. Noise

Strong noise does not pose a significant challenge for the neural network when predicting phase maps from noisy input. As shown in Figs. 4-7 and 8, the neural network can easily predict smooth and accurate phase maps even with extremely noisy input data. Fig. 8A) shows maps with simulated electrical excitation wave patterns with noise levels of  $\sigma = 0.1$ ,  $\sigma = 0.3$  and  $\sigma = 0.8$ , respectively. Panels B) and C) show the prediction accuracies obtained with different noise levels  $\sigma$  and sparsity levels  $\xi$  stated as angular accuracy and the F-score for the phase prediction and PS prediction, respectively. The map in Fig. 8B) shows that over a wide range of noise and sparsity levels the phase prediction remains above 90% angular accuracy. In particular, with non-sparse data (sparsity = 1.0), the angular accuracy stays above 95% up to noise levels of  $\sigma = 0.8$ , which corresponds to the noise level shown on the right in panel A). However, panel C) shows that the direct prediction of PS is less accurate and robust against noise. Without sparsity, the

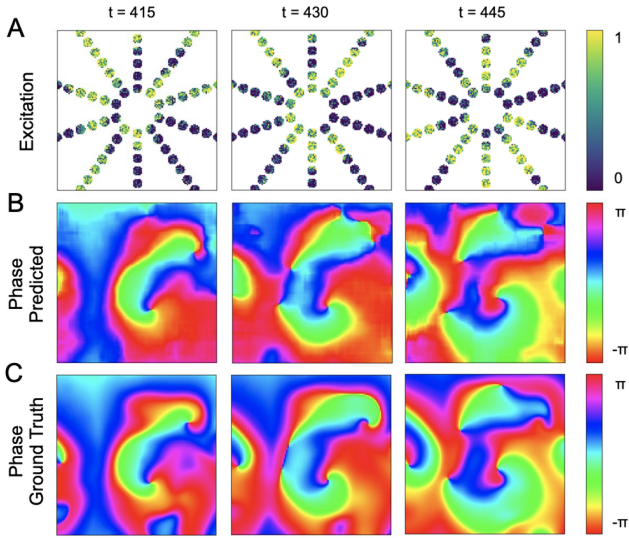


FIG. 7. Deep learning-based prediction of phase maps from sparse electrical excitation wave pattern mimicking multi-electrode catheter or optical fiber recordings. A) Sparse excitation wave pattern with noise ( $\sigma = 0.3$ , 17% coverage). B) Phase map  $\phi_p(x, y)$  predicted by neural network analyzing data in A). C) Ground-truth phase map  $\phi_g(x, y)$  obtained with complete, non-sparse, non-noisy data.

F-score does not drop below 80 with noise levels of up to  $\sigma = 0.5$ , but quickly deteriorates when both sparsity and noise reach a certain threshold (e.g. sparsity  $\xi = 0.25$  and noise  $\sigma = 0.3$ ), and even drops to 0 in extremely noisy and sparse regimes. Note that with sparsity levels of  $\xi = 0.5, 0.25, 0.125$  only every second, fourth or eight pixel of the data is seen by the network, see also next section and Fig. 9B). The systematic analysis confirms the impression given in Fig. 5C,D). The angular accuracies and F-scores shown in the maps were each computed over 5,000 frames. Even though noise degrades the prediction accuracy, overall the neural network’s phase predictions are robust and stay sufficiently accurate in the presence of strong noise. Autoencoder neural networks have excellent denoising capabilities [54, 55], and this property can be observed at work in Figs. 4 and 6-8.

### B. Sparse Data

The neural network can reconstruct phase maps from very sparse excitation data. Figs. 6 and 7 demonstrate that the neural network can predict phase maps even when the electrical input data is incomplete or sparse with measurement data lacking or available only in arbitrarily located regions or discrete measurement sites. The predicted phase maps are continuous and uninterrupted and the interpolation of phase values in between available measurement sites are sufficiently accurate. Figs. 8 and 9 elucidate this behavior in more detail. Fig. 9B) shows a sparsified electrical excitation wave pattern, where the

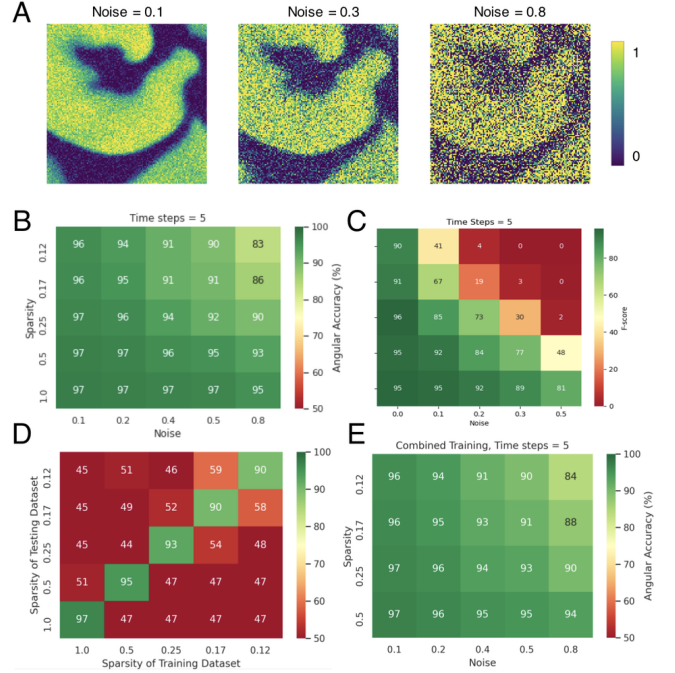


FIG. 8. Prediction accuracies with noisy and sparse data. A) Noisy simulated electrical excitation wave patterns with noise levels of  $\sigma = 0.1, 0.3, 0.8$ . B) Accurate phase predictions with strong noise and/or sparsification (with sparsity levels of 0.5 or 0.25 only every second or fourth pixel of the data is seen by the network, see also Fig. 9). Here, shown with  $N_t = 5$  sampled images, which are  $\tau = 5$  simulation time steps apart, see also Fig. 10. C) PS prediction accuracy is more sensitive to noise and sparsity and fails completely when data is both noisy and sparse. D) Neural network fails to predict phase maps accurately when applied to data with certain sparsity but was trained on data with different sparsity. E) Neural network achieves high phase prediction accuracies when training data is diverse and includes various sparsity levels.

sparsification is created by omitting all data except the data in every 8th line in  $x$ - and  $y$ -direction, respectively. This reduces the input data provided to the neural network by more than 98% to 1.6% (256 data points instead of 16,384) and corresponds to a sparsification of  $\xi = 0.125$  on the  $y$ -axis in Fig. 8B,C) and 10B,C). Correspondingly, the map in Fig. 8B) shows that the network is able to achieve phase prediction accuracies of 94–97%, even when 98% of all data is omitted and the data contains noise with noise levels of  $\sigma = 0.1 - 0.2$ . With sparsity levels of  $\xi = 0.5, 0.25, 0.125$  only every second, fourth or eight pixel of the data is seen by the network. The prediction accuracy degrades when the input is highly sparsified and noisy. However, for almost all sparsification and noise levels the phase prediction accuracy stays better than 90%. Autoencoder neural networks are very effective at interpolating image data [54, 55], and this property can be observed at work in Figs. 6-9. The phase predictions were obtained with the plain M1 network model. The PS prediction yields similar prediction

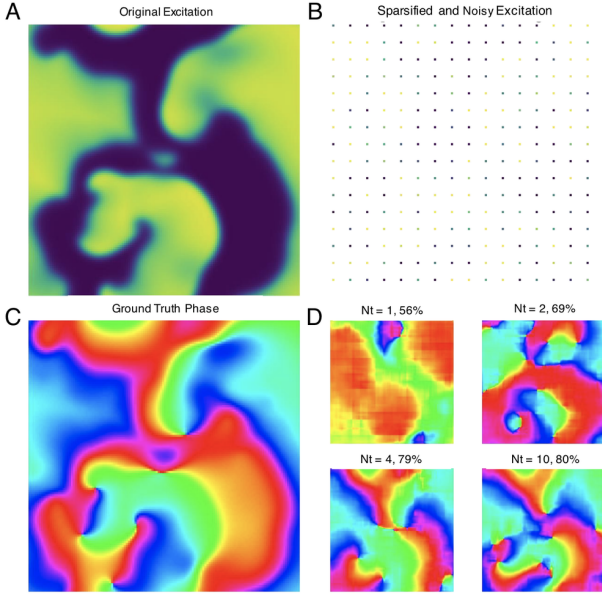


FIG. 9. Phase maps derived from very sparse and noisy electrical data using neural network. The neural network interpolates and recovers missing data by analyzing longer temporal sequences. A) Original electrical excitation wave pattern with  $128 \times 128$  pixel resolution. B) Sparsified ( $\xi = 0.125$ ) and noisy ( $\sigma = 0.8$ ) electrical excitation wave pattern with all pixels except every 8th pixel omitted (values set to 0) yielding  $16 \times 16$  non-zero data points analyzed by the neural network. Sparsity and noise levels are extreme and correspond to top right corner in plot in Fig. 8B). C) Ground-truth phase map derived from original full-resolution, non-noisy data using the Hilbert transform. D) Despite extreme sparsity and noise, the network is able to recover the corresponding phase map sufficiently well, here shown with a short sequence of  $N = 1, 2, 4, 10$  frames, respectively. The prediction gets better with longer sequences (here prediction accuracy in %, per frame). In this example, the sampled excitation snapshots are  $\tau = 5$  simulation time steps apart, see also Fig. 10.

accuracies without noise, see left column in Fig. 8C). However, with noise and sparsification, the prediction accuracy with the plain M1 network model quickly deteriorates (e.g. with  $\sigma = 0.3$  and  $\xi = 0.25$ ), highlighting that the direct PS prediction is less robust and unreliable in sparsified conditions. If the neural network is trained solely with a particular sparsification, for instance with  $\xi = 0.125$  as shown in Fig. 9B), then it fails to make predictions when analyzing data with different a sparsification. Panel D) in Fig. 8 shows how the phase prediction only works along the diagonal with test datasets that retain the same sparsification as during training. However, this issue can easily be resolved when including all sparsifications (here  $\xi = 1.0, 0.5, 0.25, 0.17, 0.125$ ) in the training dataset. The network can subsequently be applied to arbitrary sparsifications and will consistently yield phase prediction accuracies above 90%. Panel E) in Fig. 8 shows the phase prediction accuracies over noise and sparsity, as shown in panel B), but with training

performed on a broader training dataset with all sparsification levels. In B) the training was performed with each sparsification and noise level individually. The broader training in E) yields just as high phase prediction accuracies as with the narrow, specialized training (and application to one sparsification level) in B) with the advantage that the network can then be applied to arbitrary sparsification levels and not only to a particular one.

### C. Spatio-Temporal Sampling increases Accuracy and compensates Noise and Sparsity

The neural network is able to predict phase maps even with extremely noisy ( $\sigma > 0.5$ ) and extremely sparse ( $\xi > 0.25$ ) excitation data. The network typically analyzes short sequences of electrical excitation wave patterns, see also Supplementary Video 5, and is accordingly able to extract information in space and over time, see Fig. 10A). The predictions become more accurate when sampling the activity over longer times and using a short spatio-temporal sequence as input rather than just a single static excitation wave pattern, see Figs. 9D) and 10B,C). Overall, a spatio-temporal sequence rather than a static pattern as input improves the network's ability to extract information from the dynamics. Fig. 9D) shows how the prediction fails if analyzing only 1 frame with very sparse and noisy data and becomes possible when using multiple frames instead. The input is both extremely sparse ( $\xi = 0.125$ ) and extremely noisy ( $\sigma = 0.8$ ) and yet the phase maps can be predicted with an accuracy of 79% or 80% when analyzing 4 or 10 frames, respectively. In contrast, when using only 1 or 2 frames, the network does not provide reliable or sufficiently accurate predictions. The data suggests that the neural network is able to compensate information lacking in space with additional information it retrieves over time. The multi-frame analysis can also slightly improve the neural network's prediction accuracy in less extreme conditions when it is already at high accuracy levels, see Fig. 10B,C). Panel B) shows that the angular accuracy increases slightly from 93% to 97% when using  $N_t = 1, 2, 3, 4, 5$  frames for the phase prediction with low sparsity ( $\xi = 0.5$ ) and low noise ( $\sigma = 0.2$ ), respectively. We determined that  $N_t = 4 - 6$  frames is optimal and that with more frames the network's prediction accuracy saturates and does not necessarily improve much more. Panel C) shows that the F-score increases from 22% to 71%, 84%, 88% and then slightly drops to 85% when using  $N_t = 1, 3, 5, 7, 10$  frames for the PS prediction, respectively. The PS prediction appears to benefit even more from a multi-frame input. In Figs. 5-8 the results were obtained with  $N_t = 5$  frames and with the network model M1.

Interestingly, the temporal offset or spacing  $\tau$  between the excitation frames, as shown in Fig. 10A), does not appear to influence the network's ability to predict the phase maps significantly. For instance, we found that the

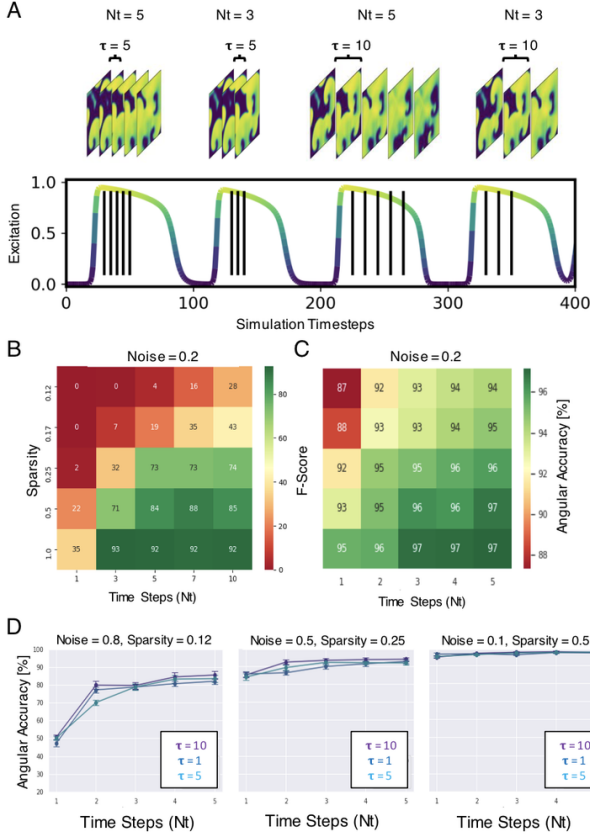


FIG. 10. Information processing with spatio-temporal data. The number of snapshots sampled from the video ( $N_t = 1, 2, 3, 4, 5, 7, 10$ ) affects the prediction accuracy, but the temporal distance between the sampled snapshots ( $\tau = 1, 5, 10$  simulation time steps) does not affect the prediction accuracy. A) Schematic drawing illustrating how much of the action potential or period of the activity is sampled with  $N_t = 3$ ,  $N_t = 5$  and  $\tau = 5$ ,  $\tau = 10$ , respectively B) Phase prediction accuracy (angular accuracy) over number of samples  $N_t$  and sparsity. More samples increase accuracy (here shown for noise  $\sigma = 0.2$ ). C) PS prediction accuracy (F-score) over number of samples  $N_t$  and sparsity. More samples increase accuracy (here shown for noise  $\sigma = 0.2$ ). D) Phase prediction accuracy does not increase or decrease with variation of temporal distance  $\tau$ .

angular accuracy did not change much when we used a temporal offset of 1, 5 or 10 simulation time steps between the sampled frames, see Fig. 10D). With  $\tau = 5$  or  $\tau = 10$  and  $N_t = 5$  frames, the dynamics are sampled over a time span of 25 or 50 simulation time steps, which corresponds to about 25% or 50% of the cycle length or dominant period of the spiral wave dynamics, respectively. This behaviour demonstrates that the neural network is able to predict phase and PS from the instantaneous dynamics rather than by associating snapshots acquired at fixed intervals over the entire phase or period of the activity. Therefore, an input parameter, such as the dominant frequency or period of the dynamics, is not required and the approach can be used with minimal

delay.

#### IV. DISCUSSION

We demonstrated that deep neural networks can be used to compute phase maps and phase singularities (PS) and provide visualizations of the topology of reentrant electrophysiological wave dynamics in cardiac tissues very accurately, robustly and almost instantaneously from a very short temporal sequence of 1-5 snapshots of the activity. The predictions do not require the collection of long time-series data and can be done in real-time using GPU hardware. We applied the phase mapping and PS detection approach to both simulated and experimental data of ventricular fibrillation (VF) and found that the neural network excels at predicting smooth phase maps under noisy conditions and can furthermore interpolate and extrapolate missing data. Consequently it can provide high-resolution phase maps from discrete measurement data obtained with sparsely distributed electrodes, arbitrary electrode configurations and arbitrary inter-electrode distances. The approach's particular strength is that it is able to simultaneously 'ignore' noise and enhance spatial resolution, which is a well-known feature of autoencoder-like convolutional neural networks [54, 55], and a feature which we explored previously in a different application when we analyzed low-resolution tissue deformation to predict electrical excitation waves [56]. With these 'superresolution', denoising and interpolation capabilities, our phase mapping and PS detection approach is ideally suited to address many of the challenges faced in phase mapping applications. While the direct prediction of PS or rotor core positions was less accurate in the presence of noise and sparsity, it is yet possible to locate PS in noisy or sparse situations indirectly by using classical methods applied to the deep learning-predicted phase maps. We demonstrated that the deep learning-based phase mapping can be applied to optical mapping data of VF and produces phase maps in real-time at imaging speeds of 500fps. If the sole objective in an optical mapping study is to visualize rotor dynamics, then our approach obviates the need for spatio-temporal smoothing and filtering, because the vortex dynamics can be visualized directly and almost instantly from the raw optical mapping data. The approach could also be applied in other fields beyond cardiovascular research when studying the dynamics of excitation waves and topological defects in other biological systems [57–60]. Lastly, our findings suggest that the approach could be used to enhance some of the computational aspects of catheter mapping and could potentially alleviate some of its shortcomings associated with misrepresenting fibrillatory wave dynamics.

One of the most critical issues with neural networks is their ability 'to generalize'. Neural networks are known to perform very well when applied to data that is very similar to or 'within the distribution' of the training

data, but their accuracy and robustness may quickly deteriorate when applied to other, less similar 'out-of-distribution' data. In Fig. 8D) and E), we showed that the same network, if trained with a more diverse dataset that includes various sparsities, can make predictions with arbitrarily sparse data, while it fails to do so if trained only on a narrow dataset with a single fixed sparsity. This anecdotal finding is exemplary for a very general property of neural networks and data driven approaches and similar observations would be made with other parameters, such as noise, blurring, arbitrary sparsification patterns or parameters which alter the wave dynamics to a point where they are out-of-distribution. Even though we did not simulate a broader spectrum of wave dynamics using multiple models or parameter sets, we chose a parameter regime which exhibits both spiral wave chaos and laminar wave dynamics to broaden the dynamics learned by the network, and the network appears to perform equally well in both dynamical regimes. We studied the effect of the training data composition onto the (cross-) prediction accuracy of an architecturally very similar neural network and made very similar observations in a previous study [56]. These findings further highlight that training datasets need to be diverse, and the more diverse and well-curated, the more robustly the network performs in various conditions, which will be important for practical applications. We anticipate that the network's generalization will not become an issue in optical mapping studies, in which the video properties are often similar or sufficiently homogeneous across studies, at least when the imaging conditions are comparable. However, if the deep learning-based phase mapping and PS detection approach is used for diagnostic purposes, e.g. during the catheter-based mapping of persistent AF, its performance needs to be evaluated very carefully from patient to patient and from one imaging device to the

other.

While the deep learning-based approach excels in noisy conditions with sparse data and provides phase predictions, which are close to the non-noisy, non-sparsified ground truth data, the approach will never be better than the ground truth and only provide predictions that are as good as the ground truth. With experimental data the ground truth needs to be calculated, as in our case with the VF data, such that the prediction can only get as accurate as the ground truth phase maps that were used during training and were derived using conventional phase mapping and phase state reconstruction techniques. Lastly, the deep learning approach is only feasible if training data is available, which is not necessarily always the case.

## V. CONCLUSIONS

We demonstrated that deep encoder-decoder convolutional neural networks can be used to predict phase maps and phase singularities of cardiac electrical wave dynamics in both simulated and experimental data. Given adequate training, convolutional neural networks are able to predict phase maps and phase singularities from a short spatio-temporal sequence of electrical excitation wave patterns comprising only 1-5 frames. The predictions can be made almost instantaneously, robustly and with very high accuracies of about 95%, and even in the presence of strong noise and highly sparse or incomplete data. We demonstrated the feasibility of the approach with voltage-sensitive optical mapping recordings of ventricular fibrillation and simulated data mimicking recordings obtained with multi-electrode catheters or fiber optics. In the future, our approach could be used in electro-anatomic mapping applications for the diagnosis of atrial fibrillation.

- 
- [1] A. T. Winfree, *Journal of Theoretical Biology* **138**, 353 (1989).
  - [2] R. A. Gray, A. M. Pertsov, and J. Jalife, *Nature* **392**, 75 (1998).
  - [3] F. X. Witkowski, L. J. Leon, P. A. Penkoske, W. R. Giles, M. L. Spano, W. L. Ditto, and A. T. Winfree, *Nature* **392**, 78 (1998).
  - [4] M. P. Nash, A. Mourad, R. H. Clayton, P. M. Sutton, C. P. Bradley, M. Hayward, D. J. Paterson, and P. Taggart, *Circulation* **114**, 536 (2006).
  - [5] K. Umapathy, K. Nair, S. Masse, S. Krishnan, J. Rogers, M. P. Nash, and K. Nanthakumar, *Circulation: Arrhythmia and Electrophysiology* **3**, 105 (2010).
  - [6] J. Christoph, M. Chebbok, C. Richter, J. Schröder-Schetelig, P. Bittihn, S. Stein, I. Uzelac, F. H. Fenton, G. Hasenfuss, R. J. Gilmour, and S. Luther, *Nature* **555**, 667 (2018).
  - [7] Y.-B. Liu, A. Peter, S. T. Lamp, J. N. Weiss, P.-S. Chen, and S.-F. Lin, *Journal of Cardiovascular Electrophysiology* **14**, 1103 (2003).
  - [8] A. V. Zaitsev, P. K. Guha, F. Sarmast, A. Kolli, O. Berenfeld, A. M. Pertsov, J. R. de Groot, R. Coronel, and J. Jalife, *Circulation Research* **92**, 546 (2003).
  - [9] M. Valderrábano, P.-S. Chen, and S.-F. Lin, *Circulation* **108**, 354 (2003).
  - [10] F. Fenton and A. Karma, *Chaos: An Interdisciplinary Journal of Nonlinear Science* **8**, 20 (1998).
  - [11] R. Clayton, E. Zhuchkova, and A. Panfilov, *Progress in Biophysics and Molecular Biology* **90**, 378 (2006), from *Funny Current to Current Physiome*.
  - [12] R. Zaritski, S. F. Mironov, and A. M. Pertsov, *Phys. Rev. Lett.* **23** (2004).
  - [13] S. Nattel, F. Xiong, and M. Aguilar, *Nature Reviews Cardiology* **14** (2017), 10.1038/nrcardio.2017.37.
  - [14] M.-A. Bray, S.-F. Lin, R. R. Aliev, B. J. Roth, and J. P. Wikwso Jr., *Journal of Cardiovascular Electrophysiology* **12**, 716 (2001).

- [15] M. Hwang, J.-S. Song, Y.-S. Lee, C. Li, E. B. Shim, and H.-N. Pak, *PLOS ONE* **11**, 1 (2016).
- [16] M. Rodrigo, A. M. Climent, A. Liberós, F. Fernández-Avilés, O. Berenfeld, F. Atienza, and M. S. Guillem, *Circulation: Arrhythmia and Electrophysiology* **10**, e005008 (2017).
- [17] P. Kuklik, S. Zeemering, B. Maesen, J. Maessen, H. J. Crijns, S. Verheule, A. N. Ganesan, and U. Schotten, *IEEE Transactions on Biomedical Engineering* **62**, 296 (2015).
- [18] P. Podziemski, S. Zeemering, P. Kuklik, A. van Hunnik, B. Maesen, J. Maessen, H. J. Crijns, S. Verheule, and U. Schotten, *Circulation: Arrhythmia and Electrophysiology* **11**, e005858 (2018).
- [19] R. Abad, O. Collart, P. Ganesan, A. J. Rogers, M. I. Alhousseini, M. Rodrigo, S. M. Narayan, and W.-J. Rappel, *PLOS ONE* **16**, 1 (2021).
- [20] A. N. Iyer and R. A. Gray, *Annals of Biomedical Engineering* **29**, 47 (2001).
- [21] M.-A. Bray and J. P. Wikswo, *Phys. Rev. E* **65**, 051902 (2002).
- [22] J. Rogers, *IEEE Transactions on Biomedical Engineering* **51**, 56 (2004).
- [23] M. Yamazaki, S. Mironov, C. Taravant, J. Brec, L. M. Vaquero, K. Bandaru, U. M. R. Avula, H. Honjo, I. Kodama, O. Berenfeld, and J. Kalifa, *Cardiovascular Research* **94**, 48 (2012).
- [24] M. S. Guillem, A. M. Climent, M. Rodrigo, F. Fernández-Avilés, F. Atienza, and O. Berenfeld, *Cardiovascular Research* **109**, 480 (2016).
- [25] E. Entcheva and H. Bien, *Progress in Biophysics and Molecular Biology* **92**, 232 (2006).
- [26] V. Muñoz, K. R. Grzeda, T. Desplantez, S. V. Pandit, S. Mironov, S. M. Taffet, S. Rohr, A. G. Kléber, and J. Jalife, *Circulation Research* **101**, 475 (2007).
- [27] M. J. You, P. Langfield, L. Campanari, M. Dobbs, A. Shrier, and L. Glass, *Chaos: An Interdisciplinary Journal of Nonlinear Science* **27**, 093938 (2017).
- [28] C. H. Roney, C. D. Cantwell, J. D. Bayer, N. A. Qureshi, P. B. Lim, J. H. Tweedy, P. Kanagaratnam, N. S. Peters, E. J. Vigmond, and F. S. Ng, *Circulation: Arrhythmia and Electrophysiology* **10**, e004899 (2017).
- [29] P. Kuklik, S. Zeemering, A. van Hunnik, B. Maesen, L. Pison, D. H. Lau, J. Maessen, P. Podziemski, C. Meyer, B. Schäffer, H. Crijns, S. Willems, and U. Schotten, *IEEE Transactions on Biomedical Engineering* **64**, 310 (2017).
- [30] B. King, A. Porta-Sánchez, S. Massé, N. Zamiri, K. Balasundaram, M. Kusha, N. Jackson, S. Haldar, K. Umaphathy, and K. Nanthakumar, *Heart Rhythm* **14**, 608 (2017).
- [31] C. Roney, A. L. Wit, and N. Peters, *Arrhythmia and Electrophysiology Review* **8**, 273–84 (2019).
- [32] R. Zou, J. Kneller, L. J. Leon, and S. Nattel, *Chaos: An Interdisciplinary Journal of Nonlinear Science* **12**, 764 (2002).
- [33] J. Christoph and S. Luther, *Frontiers in Physiology* **9**, 1483 (2018).
- [34] K. N. Aronis, R. D. Berger, and H. Ashikaga, *Circulation: Arrhythmia and Electrophysiology* **10**, e005634 (2017).
- [35] V. I. Krinsky, I. R. Efimov, and J. Jalife, *Proceedings of the Royal Society of London. Series A: Mathematical and Physical Sciences* **437**, 645 (1992).
- [36] D. Barkley, M. Kness, and L. S. Tuckerman, *Phys. Rev. A* **42**, 2489 (1990).
- [37] N. Tomii, M. Yamazaki, T. Arafune, H. Honjo, N. Shibata, and I. Sakuma, *IEEE Transactions on Biomedical Engineering* **63**, 1795 (2016).
- [38] Y.-S. Lee, J.-S. Song, M. Hwang, B. Lim, B. Joung, and H.-N. Pak, *PLOS ONE* **11**, 1 (2016).
- [39] T.-C. Li, D.-B. Pan, K. Zhou, R. Jiang, C. Jiang, B. Zheng, and H. Zhang, *Phys. Rev. E* **98**, 062405 (2018).
- [40] C. D. Marcotte and R. O. Grigoriev, *Chaos: An Interdisciplinary Journal of Nonlinear Science* **27**, 093936 (2017).
- [41] D. Gurevich, C. Herndon, I. Uzelac, F. Fenton, and R. Grigoriev (2017).
- [42] D. R. Gurevich and R. O. Grigoriev, *Chaos: An Interdisciplinary Journal of Nonlinear Science* **29**, 053101 (2019).
- [43] N. Vandersickel, E. Van Nieuwenhuysse, N. Van Cleemput, J. Goedgebeur, M. El Haddad, J. De Neve, A. Demolder, T. Strisciuglio, M. Duytschaever, and A. V. Panfilov, *Frontiers in Physiology* **10**, 1138 (2019).
- [44] M. K. Mulimani, J. K. Alageshan, and R. Pandit, *Phys. Rev. Research* **2**, 023155 (2020).
- [45] M. I. Alhousseini, F. Abuzaid, A. J. Rogers, J. A. Zaman, T. Baykaner, P. Clopton, P. Bailis, M. Zaharia, P. J. Wang, W.-J. Rappel, and S. M. Narayan, *Circulation: Arrhythmia and Electrophysiology* **13**, e008160 (2020).
- [46] X. Li, T. P. Almeida, N. Dastagir, M. S. Guillem, J. Salinet, G. S. Chu, P. J. Stafford, F. S. Schlindwein, and G. A. Ng, *Frontiers in Physiology* **11**, 869 (2020).
- [47] S. Hochreiter and J. Schmidhuber, *Neural Computation* **9**, 1735 (1997).
- [48] X. Shi, Z. Chen, H. Wang, D. Yeung, W. Wong, and W. Woo, in *Advances in Neural Information Processing Systems 28: Annual Conference on Neural Information Processing Systems 2015, December 7-12, 2015, Montreal, Quebec, Canada*, edited by C. Cortes, N. D. Lawrence, D. D. Lee, M. Sugiyama, and R. Garnett (2015) pp. 802–810.
- [49] S. Ioffe and C. Szegedy, in *Proceedings of the 32nd International Conference on Machine Learning*, Proceedings of Machine Learning Research, Vol. 37, edited by F. Bach and D. Blei (PMLR, Lille, France, 2015) pp. 448–456.
- [50] V. Nair and G. E. Hinton (Omnipress, Madison, WI, USA, 2010) p. 807–814.
- [51] M. Abadi, A. Agarwal, P. Barham, E. Brevdo, Z. Chen, C. Citro, G. S. Corrado, A. Davis, J. Dean, M. Devin, S. Ghemawat, I. Goodfellow, A. Harp, G. Irving, M. Isard, Y. Jia, R. Jozefowicz, L. Kaiser, M. Kudlur, J. Levenberg, D. Mané, R. Monga, S. Moore, D. Murray, C. Olah, M. Schuster, J. Shlens, B. Steiner, I. Sutskever, K. Talwar, P. Tucker, V. Vanhoucke, V. Vasudevan, F. Viégas, O. Vinyals, P. Warden, M. Wattenberg, M. Wicke, Y. Yu, and X. Zheng, “TensorFlow: Large-scale machine learning on heterogeneous systems,” <https://www.tensorflow.org> (2015).
- [52] R. R. Aliev and A. V. Panfilov, *Chaos, Solitons & Fractals* **7**, 293 (1996).
- [53] D. P. Kingma and J. Ba, in *3rd International Conference on Learning Representations, ICLR 2015, San Diego, CA, USA, May 7-9, 2015, Conference Track Proceedings*, edited by Y. Bengio and Y. LeCun (2015).
- [54] P. Vincent, H. Larochelle, Y. Bengio, and P.-A. Manzagol (Association for Computing Machinery, 2008) p. 1096–1103.
- [55] L. Gondara (arXiv:1608.04667v2, 2016).

- [56] J. Christoph and J. Lebert, *Chaos: An Interdisciplinary Journal of Nonlinear Science* **30**, 123134 (2020).
- [57] X. Huang, W. Xu, J. Liang, K. Takagaki, X. Gao, and J. young Wu, *Neuron* **68**, 978 (2010).
- [58] D. Taniguchi, S. Ishihara, T. Oonuki, M. Honda-Kitahara, K. Kaneko, and S. Sawai, *Proceedings of the National Academy of Sciences* **110**, 5016 (2013).
- [59] T. Tan, J. Liu, P. Miller, M. Tekant, J. Dunkel, and N. Fakhri, *Nat. Phys.* **16**, 657–662 (2020).
- [60] J. Liu, J. F. Tetz, P. W. Miller, A. D. Hastewell, Y.-C. Chao, J. Dunkel, and N. Fakhri, *Proceedings of the National Academy of Sciences* **118** (2021), 10.1073/pnas.2104191118.

## Appendix A: Supplementary Video Annotations

Supplementary Videos are available online at [gitlab.com/janlebert/phasetnet-supplementary-materials-arxiv](https://gitlab.com/janlebert/phasetnet-supplementary-materials-arxiv).

**Supplementary Movie 1:** Neural network predictions of phase maps from voltage-sensitive optical mapping video data. The recording shows action potential spiral vortex waves during ventricular fibrillation on the left ventricular surface of a porcine heart, see also Fig. 4. The pixel-wise normalized transmembrane voltage is shown on the left (yellow: depolarized, blue: repolarized tissue). Center: smoothed ground truth phase map, which was obtained from the noisy optical maps using the Hilbert transform, see Fig. 3A) and section IIB. Right: phase map predicted by the neural network.

**Supplementary Movie 2:** Phase singularities (PS) predicted by the neural network from (sparse) simulated electrical spiral wave chaos without and with noise ( $\sigma = 0.2$ , see also Fig. 5). Left: ground truth electrical excitation, Center: noisy and sparse network input ( $N_t = 5$ ), Right: predicted PS (black) and true PS (white) superimposed onto the corresponding electrical excitation wave maps.

**Supplementary Movie 3:** Phase maps predicted by the neural network from (sparse) simulated electrical excitation wave maps without and with noise ( $\sigma = 0.3$ ), see section . Left: electric excitation wave maps uses as network input ( $N_t = 5$ ). Center: ground truth or true phase. Right: neural network output.

**Supplementary Movie 4:** Phase maps predicted by the neural network from (sparse) simulated electrical excitation wave maps without and with noise ( $\sigma = 0.3$ ) for  $N_t = 5$ .

**Supplementary Movie 5:** Neural network prediction of a single phase map. The 5 noisy and sparse electrical wave frames provided to the neural network as input, as well as the predicted phase map and the true phase map.